Supplementary Information: *Large effect on liquid midlatitude frontal cloud albedo from Aitken-mode aerosols*

Muhammad Mueed Khan[1,2], J. Christine Chiu[3], Han Ding[1,2], Pratapaditya Ghosh[1,4], August Mikkelsen[5], Daniel McCoy[5], Jian Wang[6], Xuemei Wang[1,7], Masaru Yoshioka[8], Damao Zhang[9], Hamish Gordon[1,10]*

[1]Center for Atmospheric Particle Studies, Carnegie Mellon University, 5000 Forbes Ave, Pittsburgh, 15213, PA, USA.
[2]Department of Mechanical Engineering, Carnegie Mellon University, 5000 Forbes Ave, Pittsburgh, 15213, PA, USA.
[3]Department of Atmospheric Science, Colorado State University, 711 Oval Drive, Fort Collins, 80521, CO, USA.
[4]Atmospheric, Earth, & Energy Division, Lawrence Livermore National Laboratory, 7000 East Avenue, Livermore, 94550, CA, USA.
[5]Department of Atmospheric Science, University of Wyoming, 1000 E University Ave, Laramie, 82072, WY, USA.
[6]Center for Aerosol Science and Engineering, Washington University in St Louis, One Brookings Drive, St. Louis, 63130, MO, USA.
[7]Koninklijk Nederlands Meteorologisch Instituut, 3730 AE, De Bilt, 3731 GA, Utrecht, Netherlands.
[8]School of Earth and Environment, University of Leeds, Woodhouse Lane, Leeds, LS2 9JT, UK.
[9]Pacific Northwest National Laboratory, 902 Battelle Boulevard, Richland, 99352, WA, USA.
[10]Department of Chemical Engineering, Carnegie Mellon University, 5000 Forbes Ave, Pittsburgh, 15213, PA, USA.

*Corresponding author(s). E-mail(s): gordon@cmu.edu;
Contributing authors: mueedkhan@cmu.edu;
Christine.Chiu@colostate.edu; handing@andrew.cmu.edu;

ghosh9@llnl.gov; amikkels@uwyo.edu; daniel.mccoy@uwyo.edu;
jian@wustl.edu; xuemeiwa@andrew.cmu.edu; M.Yoshioka@leeds.ac.uk;
damao.zhang@pnnl.gov;

1 Evaluation of Surface Aerosols as Proxies for Cloud-Base Aerosol Concentrations

In our analysis, we assume that ground-based aerosol measurements can serve as reliable proxies for cloud-based aerosol concentrations. This assumption, while not commonly adopted in literature, is necessary here because marine frontal clouds, especially when supercooled, are often avoided by research aircraft due to safety (icing risk) and sampling constraints. Moreover, in situ aerosol instruments aboard aircraft often require cloud masking to avoid contamination by cloud droplets, unless equipped with a counterflow virtual impactor (CVI). Previous research has used various ground-based sensors to infer cloud-relevant aerosol properties, such as extinction from Raman lidar measurements [1–5]. However, lidar extinction is highly sensitive to atmospheric humidity, and is most sensitive to the presence of large accumulation and coarse mode particles, and has only limited sensitivity to the smallest aerosols that might activate in frontal clouds, in the Aitken mode.

Therefore, we first compared UHSAS surface aerosol number concentrations greater than 60 nm in diameter, N_{60}, with surface aerosol concentrations in our regional UM simulations across all four cases. Our analysis shows the model performs well: there is a strong correlation between UHSAS surface measurements and UM-modeled surface aerosol concentrations, with $R^2 = 0.83$ and normalized mean bias (NMB) $\approx -6\%$ (main text Fig. 1(b)). We then compared vertical profiles of N_{60} from the UM with in situ measurements from the FIMS instrument onboard the aircraft a few hours before and after a frontal cloud passage during the ACE-ENA campaign (Fig. 1(c)). The model captures the vertical structure of the aerosol profile reasonably well, though not perfectly: near the surface, the model underestimates N_a relative to the FIMS by 11–19%, whereas aloft, particularly between 1200 m and 2000 m, the model overpredicts concentrations by 8–14%. The overprediction of new particle formation in the free and upper troposphere is a known bias in this model [6]. Nevertheless, these discrepancies are small relative to most aerosol modeling studies in the remote marine atmosphere [e.g. 7] and to other uncertainties in this study such as those in the N_d retrievals. We conclude that the UM simulations can be used to test the assumption that surface-based aerosol measurements provide a first-order estimate of cloud-base conditions.

With confidence that the simulations are reasonable, we assessed the consistency between simulated aerosol concentrations at the surface and at cloud base to evaluate whether surface observations can reasonably approximate aerosol concentrations relevant to cloud microphysical properties. Time series comparisons for a cyclone case in May 2017 (main text Fig. 1(a), lower panel) indicate that simulated surface and cloud-base aerosol concentrations mostly agree within 50%, but not always. A more systematic evaluation (Fig. S1) shows that discrepancies increase with cloud-base height, reaching an average ±100% difference for the highest cloud bases (>1.6 km). To minimize uncertainties in aerosol activation and cloud albedo sensitivity analyses, we therefore restrict our dataset for these studies to intermediate cloud-base heights (0.3–1.1 km), where differences remain within ±50%. Approximately 71% of our sampled cloud bases are at these lower altitudes, as shown in Fig. 1(d).

The correlation between simulated surface and simulated cloud-base N_{60} in cold front clouds has an R^2 of 0.82 (Fig. 1(e)). However, aerosols at cloud base altitudes are systematically 25% higher than aerosols at the surface. It is possible that aerosols near the surface are more susceptible to turbulent deposition, leading to greater losses. Alternatively or in addition, coarse-mode sea spray aerosols at the surface scavenge condensable vapors and likely inhibit new particle formation. In the upper boundary layer, new particle formation becomes more likely [8], leading to increased aerosol number concentrations. Strong vertical mixing in cold fronts would mitigate, but not eliminate, this effect by redistributing both sea spray and newly formed particles. We test a correction for this discrepancy.

In warm and non-frontal clouds, correlation between surface and cloud base N_{60} is weaker. In non-frontal clouds, $R^2 = 0.56$, and aerosols at cloud base are 16% lower than aerosols at the surface (Fig. 2(g)). In warm frontal clouds, $R^2 = 0.45$ but there is no significant systematic difference between concentrations (Fig. 2(f)). The low correlation limits the potential for surface aerosol observations to yield insights into activation in these systems. While we still use the observational analysis in warm front clouds, we rely more heavily on results from our model simulations in which we use cloud base aerosol to evaluate aerosol activation and albedo response.

Taken together, these analyses support the use of surface aerosol concentrations as a proxy for cloud-base concentrations in cold front clouds and in clouds with bases below 1.1 km altitude. For non-frontal clouds with similarly low base height, the correlation between surface and cloud-base aerosol number is also reasonable and raises R^2 to 0.62. Our model evaluation also gives confidence in the ability of the model to represent aerosol concentrations in frozen or precipitating clouds, which could be a topic for future studies.

2 Alternative determination of activation diameter using Hoppel minima

Hoppel minima, the characteristic drop in aerosol size distributions between 50 and 150 nm (and visible in Fig. S8), indicate prior aerosol activation to cloud droplets. The location of the minimum can be used to infer the activation diameter [9]. Hoppel minima are usually considered in non-frontal clouds, due to the high probability that aerosols are removed by precipitation in frontal clouds instead of the clouds evaporating. However, we are able to identify some Hoppel minima that are likely due to processing of aerosol by frontal clouds. We identify candidate Hoppel minima in SMPS size distributions by calculating the mean aerosol concentration in 60-minute segments and selecting the particle size bin corresponding to the lowest mean concentration within the 35–150 nm diameter range, provided this bin is not close to the extrema of the range. Figure S17 shows the approach. White spaces indicate data removed during rain, clear sky and contamination events as described in main text Section 1.3-1.4.

Hoppel minima were detected in 9 out of the 24 frontal passages with available SMPS data (from a total of 50 cyclone cases). From these 9 frontal passages, we have 131 hours of SMPS data, and we compare the Hoppel minima in these hourly means with the minima in 216 hourly means of non-frontal cloud data. We show a histogram of the Hoppel minimum diameter in the frontal and non frontal cases in Fig. S18. Among the frontal clouds, 49 instances (37%) have minima below the smallest value observed in the non-frontal sample; 53 (41%) fall within the non-frontal range but below the non-frontal median; and 29 (22%) exceed the non-frontal median. Thus, 78% of frontal cases exhibit smaller Hoppel minima than typical non-frontal conditions. Comparatively, as shown in Fig. 3(a–c), the integral method yields activation diameters of 65–150 nm in non-frontal clouds, whereas frontal clouds showing size ranges between 55-170nm. Similar numbers are seen from the histogram of Hoppel minima (Fig. S18) where non-frontal minima most frequently exist near 90–140 nm, while frontal cases systematically extend to lower values of 40-120 nm.

The Hoppel minimum approach to activation diameters involves several important uncertainties. The Hoppel minimum represents a signature of past cloud processing rather than an instantaneous activation event. While its presence confirms that activation and subsequent condensational growth occurred, it is difficult to directly link the observed minimum to a specific frontal cloud passage. The aerosol size distribution measured at the surface may be significantly altered by scavenging, sedimentation, coagulation, or condensational growth after cloud processing. However, these uncertainties are relatively uncorrelated with that of the UHSAS–NDROP-based activation estimates discussed previously.

Table S1: Regression parameters derived from SEVIRI observation plots shown in Figures S6, and S9. For $\left(\frac{\partial\alpha}{\partial \ln N_d}\right)_{\mathbf{LWP}}$ and $\left(\frac{\partial\alpha}{\partial \ln \mathbf{LWP}}\right)_{N_d}$, a multiple linear regression $\alpha = d + m_1 \ln N_d \ + m_2 \ln LWP$ is performed from Figure S9. Here, d = 0.5 for cold front, 0.3 for warm front and 0.1 for non frontal clouds. The resulting slopes (m_1 and m_2) quantify the albedo susceptibilities with respect to N_d and LWP respectively, and together with the fits of $\frac{d\ln \mathbf{LWP}}{d\ln N_d}$ and $\frac{d\ln N_d}{d\ln N_{60}}$ from Figure S6, yield the total albedo response of $\frac{d\alpha}{d\ln N_{60}}$.

Cloud Type	$\frac{d\alpha}{d\ln N_a}$	$\left.\frac{\partial\alpha}{\partial\ln N_d}\right\rvert_{\mathrm{LWP}}$	$\left.\frac{\partial\alpha}{\partial\ln \mathrm{LWP}}\right\rvert_{N_d}$	$\frac{d\ln \mathrm{LWP}}{d\ln N_d}$	$\frac{d\ln N_d}{d\ln N_a}$
Cold front	0.020	0.041	0.079	-0.22	0.85
Warm front	0.021	0.048	0.098	-0.21	0.77
Non frontal	0.023	0.057	0.133	-0.17	0.68

Table S2: Linear regression parameters derived from the fits shown in Figures S11 and S12. For $\left(\frac{\partial\alpha}{\partial \ln N_d}\right)_{\mathbf{LWP}}$, the relationship $Y = d + m \ln X$ is applied, where Y is the cloud albedo (α) and X is the droplet number concentration (N_d) within each liquid water path (LWP) bin. Here, d = 0.6 for cold front, 0.4 for warm front and 0.2 for non frontal clouds. For $\left(\frac{\partial\alpha}{\partial \ln \mathbf{LWP}}\right)_{N_d}$, the same regression line equation is used, where Y again represents cloud albedo but X now is the LWP for a given N_d bin. Here, d = 0.5 for cold front, 0.3 for warm front and 0.1 for non frontal clouds. The resulting slopes (m) quantify the albedo susceptibilities with respect to N_d and LWP, and together with $\frac{d\ln \mathbf{LWP}}{d\ln N_d}$ from fig. S10 and $\frac{d\ln N_d}{d\ln N_{60}}$ from fig. 2 in main text, yield the total albedo response $\frac{d\alpha}{d\ln N_{60}}$.

Type	$\frac{d\alpha}{d\ln N_a}$	$\left(\frac{\partial\alpha}{\partial\ln N_d}\right)_{\mathrm{LWP}}$			$\left(\frac{\partial\alpha}{\partial\ln \mathrm{LWP}}\right)_{N_d}$			$\frac{d\ln LWP}{d\ln N_d}$	$\frac{d\ln N_d}{d\ln N_a}$
		50-100	100-150	150-200	50-100	100-150	150-200		
Cold front	0.029	0.053	0.053	0.047	0.079	0.078	0.076	-0.25	0.89
Warm front	0.033	0.062	0.061	0.061	0.089	0.088	0.086	-0.22	0.80
Non frontal	0.041	0.084	0.082	0.081	0.115	0.111	0.125	-0.18	0.71

Table S3: Regression parameters derived from surface observation plots shown in Figures S3, S13, and S15 for clouds with maximum column KaZR reflectivity of Z <-15 dBZ (non-precipitating clouds only). The susceptibilities $\left(\frac{\partial\alpha}{\partial \ln N_d}\right)_{\mathbf{LWP}}$ and $\left(\frac{\partial\alpha}{\partial \ln \mathbf{LWP}}\right)_{N_d}$ are estimated from multiple linear regression, $\alpha = d + m_1 \ln N_d + m_2 \ln LWP$ from Figure 13. Here, d = 0.5 for cold front, 0.3 for warm front and 0.1 for non frontal clouds. The resulting slopes (m_1 and m_2) quantify the albedo susceptibilities with respect to N_d and LWP respectively, and, together with power-law fit of $\frac{d \ln \mathbf{LWP}}{d \ln N_d}$ in fig. S15 and of $\frac{d \ln N_d}{d \ln N_{60}}$ in fig. S3, yield the total albedo response $\frac{d\alpha}{d \ln N_{60}}$.

Cloud Type	$\frac{d\alpha}{d\ln N_{60}}$	$\left.\frac{\partial\alpha}{\partial\ln N_d}\right\|_{\text{LWP}}$	$\left.\frac{\partial\alpha}{\partial\ln \text{LWP}}\right\|_{N_d}$	$\frac{d\ln\text{LWP}}{d\ln N_d}$ (95% CI)	R^2	$\frac{d\ln N_d}{d\ln N_{60}}$
Cold front	0.014	0.044	0.094	−0.31 [−0.39, −0.22]	0.27	0.94
Warm front	0.015	0.052	0.106	−0.32 [−0.44, −0.19]	0.18	0.84
Non-frontal	0.018	0.065	0.145	−0.28 [−0.35, −0.16]	0.22	0.72

Table S4: Regression parameters derived from surface observation plots shown in Figures S4, S14, and S16 for clouds with maximum column KaZR reflectivity of -15< Z <0 dBZ (drizzling clouds only). The susceptibilities $\left(\frac{\partial\alpha}{\partial \ln N_d}\right)_{\mathbf{LWP}}$ and $\left(\frac{\partial\alpha}{\partial \ln \mathbf{LWP}}\right)_{N_d}$ are estimated from multiple linear regression, $\alpha = d + m_1 \ln N_d + m_2 \ln LWP$ from Figure S14. Here, d = 0.5 for cold front, 0.3 for warm front and 0.1 for non frontal clouds. The resulting slopes (m_1 and m_2) quantify the albedo susceptibilities with respect to N_d and LWP respectively, and, together with power-law fit of $\frac{d \ln \mathbf{LWP}}{d \ln N_d}$ in fig. S16 and of $\frac{d \ln N_d}{d \ln N_{60}}$ in fig. S4, yield the total albedo response $\frac{d\alpha}{d \ln N_{60}}$.

Cloud Type	$\frac{d\alpha}{d\ln N_{60}}$	$\left.\frac{\partial\alpha}{\partial\ln N_d}\right\|_{\text{LWP}}$	$\left.\frac{\partial\alpha}{\partial\ln \text{LWP}}\right\|_{N_d}$	$\frac{d\ln\text{LWP}}{d\ln N_d}$ (95% CI)	R^2	$\frac{d\ln N_d}{d\ln N_{60}}$
Cold front	0.031	0.049	0.111	−0.12 [−0.23, +0.02]	0.18	0.87
Warm front	0.033	0.058	0.126	−0.11 [−0.17, +0.01]	0.13	0.77
Non-frontal	0.034	0.071	0.164	−0.13 [−0.19, −0.03]	0.15	0.69

Table S5: Sensitivity analysis of droplet number concentration susceptibility (the 'c' parameter) $\frac{d \ln N_d}{d \ln N_{60}}$ to aerosol number concentration perturbations. The 'Baseline' column represents using $\mathbf{N}_{60}$ from surface UHSAS observations, while the '+25%' column shows the effect of increasing aerosol number concentration by 25%. Surface observations of aerosol number concentration were found to underrepresent cloud base aerosol concentration in cold front clouds, as shown in Fig. 2 of the main text.

Condition	Baseline	+25%
Cold front	0.89	0.74
Warm front	0.80	0.65
Non front	0.71	0.57

Table S6: Sensitivity analysis of cloud albedo susceptibility $\frac{\alpha}{d\ln N_{60}}$ to surface aerosol number concentration when incremented by 25%. For $\left(\frac{\partial\alpha}{\partial\ln N_d}\right)_{\mathbf{LWP}}$ and $\left(\frac{\partial\alpha}{\partial\ln \mathbf{LWP}}\right)_{N_d}$, a multiple linear regression $\alpha = d + m_1 \ln N_d \; + m_2 \ln LWP$ is performed. Here, d = 0.5 for cold frontal, 0.3 for warm frontal and 0.1 for non frontal clouds. The resulting slopes (m_1 and m_2) quantify the albedo susceptibilities with respect to N_d and LWP respectively, and, together with the power-law fit of $\frac{d\ln \mathbf{LWP}}{d\ln N_d}$ and another power-law fit of $\frac{d\ln N_d}{d\ln N_{60}}$, yield the total albedo response $\frac{d\alpha}{d\ln N_{60}}$.

Cloud Type	$\frac{d\alpha}{d\ln N_a}$	$\left.\frac{\partial\alpha}{\partial\ln N_d}\right\vert_{\mathrm{LWP}}$	$\left.\frac{\partial\alpha}{\partial\ln \mathrm{LWP}}\right\vert_{N_d}$	$\frac{d\ln \mathrm{LWP}}{d\ln N_d}$	$\frac{d\ln N_d}{d\ln N_a}$
Cold front	0.017	0.049	0.104	-0.25	0.74
Warm front	0.019	0.057	0.121	-0.22	0.65
Non frontal	0.022	0.068	0.163	-0.18	0.57

Table S7: 50 cases of frontal cloud passages over Graciosa Island. The averaged aerosol number concentration (N_{60}) represents particles with diameters larger than 60 nm, measured at the surface at the ARM site. Values reported are mean concentrations over the duration of the frontal cloud passage (some periods span multiple days). Sea-level pressure (SLP) is given as a representative single reading of the minimum central pressure of the cyclone system when it was closest to or directly affecting the ARM site, and is used here as a simple indicator of the strength of the cyclone. "Shape/Quality" subjectively describes the morphology of the cloud system in satellite imagery. 'Skewed' indicates warm and cold frontal clouds are passing one after another very closely, or less clearly organized. 'Clean' indicates a cyclone with a clear comma shape and isolated fronts. 'Choppy' indicates broken or patchy frontal cloud structure. "Front Passage" identifies whether a warm, cold, or both fronts were captured at the ENA site. Occluded fronts are counted as cold fronts. "Instances" notes whether the cyclone was fully within the SEVIRI field of view or only partially observed.

No.	**Date & Time (UTC)**	**Avg N_{60} cm^{-3}**	**Shape/ Quality**	**Front Passage**	**SLP (hPa)**	**Instances**
1	Jan 18 2017 05:07–10:00 hrs	161	Spiral	Cold front	980	All
2	Jan 19 2017 14:00–22:45 hrs	253	Huge spiral	Cold front	992	uncertain (2 storms)
3	Jan 20 2017 00:00–Jan 21 01:30 hrs; Jan 22 14:00–Jan 25 00:00 hrs	202	Spiral	Warm & Cold front	972	Out of SEVIRI view (forms)
4	Jan 26 2017 12:00–Jan 30 01:30 hrs	130	Developing/ receding spiral	Warm & Cold front	990	Partial on 29th
5	Jan 31 2017 08:45–Feb 01 16:00 hrs	210	Spiral	Warm & Cold front	962	Partial (1st Feb only)
6	Feb 04 2017 20:00–Feb 06 05:30 hrs	140	Spiral	Cold front	960	On 6th but out of SEVIRI view
7	Feb 13 2017 15:00–Feb 14 15:00 hrs; Feb 15 21:00–Feb 16 17:00 hrs	120	Skewed, multiple cyclones	Cold front	994	–
8	Feb 22 2017 15:30–Feb 23 02:20 hrs; Feb 24 11:00–Feb 25 01:00 hrs	213	possible warm front	Cold & warm front	990	Momentarily on 24th
9	Mar 02 2017 23:00–Mar 04 10:45 hrs	332	Large spiral	Warm front	965	–

(Continued on next page)

(Continued from prev. page)

No.	**Date & Time (UTC)**	**Avg** N_{60} **cm**$^{-3}$	**Shape/ Quality**	**Front Passage**	**SLP (hPa)**	**Instances**
10	Mar 06 2017 06:30–Mar 09 15:35 hrs	220	Large skewed	Cold front	992	Partial only on 6th
11	Mar 15 2017 10:30–17:00 hrs	88	Spiral	Cold front	999	–
12	Mar 26 2017 05:00–Mar 27 16:30 hrs	143	Captures cold sector	Cold front	1002	–
13	Aug 22 2017 01:00–22:00 hrs	131	Spiral (tail end only)	Cold front	991	–
14	Apr 28 2017 20:00–Apr 29 12:30 hrs	287	–	Cold front	977	On 28th but out of SEVIRI view
15	Apr 30 2017 09:00–May 02 13:00 hrs	305	Spiral	Cold front	975	–
16	May 12 2017 12:00–May 14 18:00 hrs	180	Spiral	Warm & Cold front	985	–
17	May 20 2017 09:00–23:30 hrs; May 22 08:00–12:00 hrs; May 23 03:00–16:00 hrs	340	Spiral—successive cyclones	Warm & Cold front	989	–
18	May 25-26 2017 13:00–18:00 hrs	120	Spiral	Cold & Warm front	1000	Warm front passing at night
19	May 31 2017 04:00–Jun 01 06:30 hrs	210	Large spiral	Cold front	986	–
20	Jun 03 2017 18:00–Jun 05 15:00 hrs	184	Large skewed	Warm & Cold front	996	–
21	Jun 06 2017 15:00–Jun 07 15:00 hrs	217	Skewed	Cold front	994	–
22	Jun 08 2017 00:00–23:30 hrs	230	Spiral, lightly crossing warm front	Warm & Cold front	965	On 10th, >1 low-pressure system
23	Jun 13 2017 12:00–Jun 14 20:00 hrs	198	Large spiral (tail end only)	Cold front	980	–

(Continued on next page)

(Continued from prev. page)

No.	Date & Time (UTC)	Avg N_{60} cm^{-3}	Shape/ Quality	Front Passage	SLP (hPa)	Instances
24	Jun 18 2017 08:30–17:00 hrs	329	Spiral, cold front tail	Cold front	1001	–
25	Jul 07 2017 23:00–Jul 08 04:30 hrs	315	spiral	Cold front	986	–
26	Jul 31 2017 00:00–Aug 01 08:00 hrs; Aug 03 08:00–Aug 05 12:00 hrs	164	Ahead of warm front	Cold front	992	1st Aug only
27	Aug 20 2017 18:00–Aug 21 22:00 hrs	176	Large spiral	Cold front	987	–
28	Sep 04 2017 03:00–18:00 hrs	147	Large spiral	Cold front	1001	–
29	Sep 19 2017 16:00–Sep 20 08:00 hrs	167	Large spiral, skewed	Cold front	1003	–
30	Sep 22 2017 12:00–22:00 hrs	138	Clean spiral ahead of warm front	Cold and Warm front	976	–
31	Sep 28 2017 04:00–15:00 hrs	253	Spiral	Cold front	990	–
32	Oct 13 2017 23:20–Oct 14 15:00 hrs	343	Large spiral	Cold front	981	Out of SEVIRI view
33	Oct 19 2017 21:00–Oct 20 03:00 hrs	212	Spiral	Cold front	984	–
34	Oct 21 2017 09:00–Oct 22 06:00 hrs; Oct 23 00:00–Oct 24 08:00 hrs	139	Large spiral with cold front)	Warm & Cold front	972	Few instances SEVIRI
35	Nov 04 2017 15:00–Nov 05 08:00 hrs; Nov 06 03:00–Nov 07 21:00 hrs	148	Large spiral	Cold and Warm front	999	–
36	Nov 17 2017 00:00–04:30 hrs; Nov 17 09:00–Nov 18 17:00 hrs	122	Very thick cold fronts, twin cyclones	Cold front	996	–
37	Nov 19 2017 03:00–Nov 20 10:30 hrs	117	Very thick fronts	Cold front	982	Only on 20
38	Nov 23 2017 00:00–Nov 24 18:00 hrs	110	open cells but spiral	Warm front	985	–
39	Nov 30 2017 00:00–21:00 hrs	118	Warm front north-facing, spiral	Cold front	998	–

(Continued on next page)

(Continued from prev. page)

No.	Date & Time (UTC)	Avg N_{60} cm^{-3}	Shape/ Quality	Front Passage	SLP (hPa)	Instances
40	Dec 04 2017 01:30–22:00 hrs	95	Spiral	Cold and warm front	990	–
41	Dec 06 2017 00:00–23:30 hrs	163	Skewed shape	Warm front	993	–
42	Dec 19 2017 00:00–21:00 hrs	195	Large spiral	Cold front	1000	–
43	Jan 04 2018 08:00–18:00 hrs	164	Large skewed spiral	Cold front	1005	Out of SEVIRI sight
44	Jan 11 2018 05:00–18:00 hrs	189	Large skewed and twin cyclone	Cold front	999	Out of SEVIRI sight
45	Feb 13 2018 13:00–23:00 hrs; Feb 14 2018 13:00–24:00 hrs	53	Large spiral	Warm & Cold front	1004	Out of SEVIRI sight
46	Mar 05 2018 00:00–Mar 06 16:00 hrs; Mar 06 17:30–Mar 07 09:00 hrs; Mar 07 20:00–23:30 hrs	126	large cyclone	Warm & Cold front	1001	–
47	Mar 30 2018 09:00–Mar 31 08:00 hrs	113	Skewed spiral	Cold and warm front	985	Only 30–31 Mar
48	Apr 12 2018 12:00–Apr 13 12:00 hrs; Apr 13 19:00–Apr 14 11:00 hrs	182	spiral	Warm & Cold front	978	–
49	Apr 21 2018 12:00–Apr 22 14:00 hrs; Apr 24 06:00–21:00 hrs	190	Large spiral	Warm & Cold front	996	capture periphery of warm front
50	Jun 05 2018 04:00–23:30 hrs	119	Spiral	Cold front	980	warm front KaZR unavailable

Table S8: Non-frontal low-level cloud search periods over ARM ENA site.

Case	Start (UTC)	End (UTC)
1	2017-01-05 03:00	06:00
2	2017-02-02 00:00	14:00
3	2017-02-14 11:00	15:00
4	2017-03-21 12:00	15:00
5	2017-04-07 12:00	14:00
6	2017-04-25 07:00	09:00
7	2017-05-25 00:00	19:00
8	2017-06-04 00:00	18:00
9	2017-06-17 13:00	18:00
10	2017-07-07 08:00	15:00
11	2017-07-21 05:00	19:00
12	2017-08-03 07:00	11:00
13	2017-08-29 00:00	18:00
14	2017-09-03 14:00	19:00
15	2017-09-21 08:00	18:00
16	2017-10-08 00:00	20:00
17	2017-10-23 06:00	10:00
18	2017-11-08 05:00	08:00
19	2017-12-02 01:00	20:30
20	2017-12-21 15:00	19:00
21	2018-01-05 10:00	14:00
22	2018-01-27 00:00	13:00
23	2018-02-10 00:00	01:00
23	2018-02-10 07:00	08:00
24	2018-02-24 05:00	07:00
25	2018-03-02 01:00	03:30
25	2018-03-02 16:00	19:00
26	2018-03-28 00:00	14:00
27	2018-04-14 12:00	01:00
28	2018-04-27 07:00	13:00
29	2018-05-03 09:00	18:00
30	2018-05-21 14:00	17:00
31	2018-06-08 18:00	19:00
32	2018-06-23 00:00	21:00
33	2018-07-09 16:00	17:00
33	2018-07-09 21:00	18:30
34	2018-07-20 02:00	07:00
35	2018-08-01 12:00	14:00
36	2018-08-13 01:00	06:00
36	2018-08-13 10:00	15:00
37	2018-08-25 07:00	10:30
38	2018-09-05 09:00	13:00
39	2018-09-18 02:00	16:00
40	2018-09-25 09:00	12:00
41	2018-10-12 18:00	19:00
42	2018-10-25 05:00	15:00
43	2018-11-04 07:00	10:00
44	2018-11-17 12:00	15:00
45	2018-11-28 20:00	19:00
46	2018-12-02 09:00	10:00
47	2018-12-04 15:00	19:00
48	2018-12-12 10:00	17:00
49	2018-12-15 12:00	19:00
50	2018-12-31 09:00	12:00

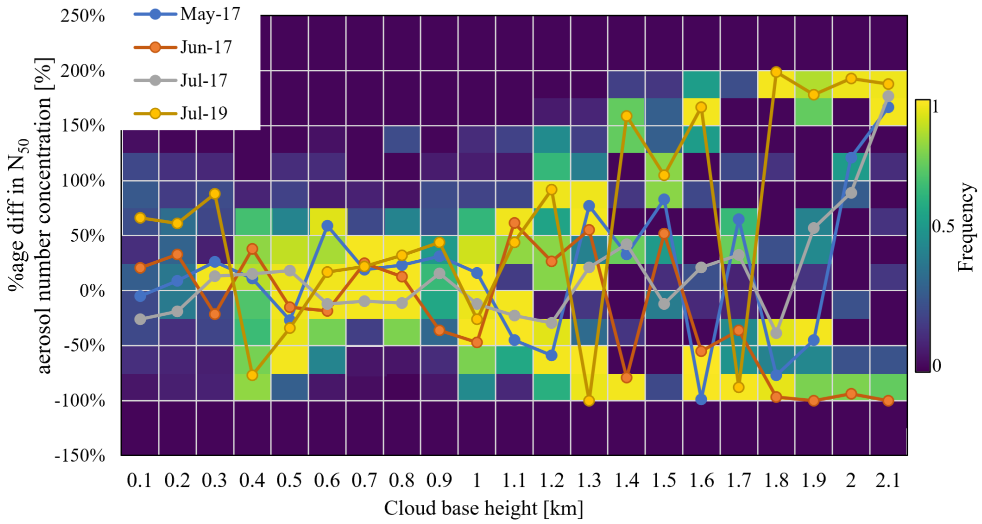

Figure S1: Percentage differences between simulated aerosol concentrations at cloud base and simulated aerosol concentrations at the surface, as a function of the altitude of the cloud base. The histogram shows the four simulated cases while lines show mean for each cyclone separately.

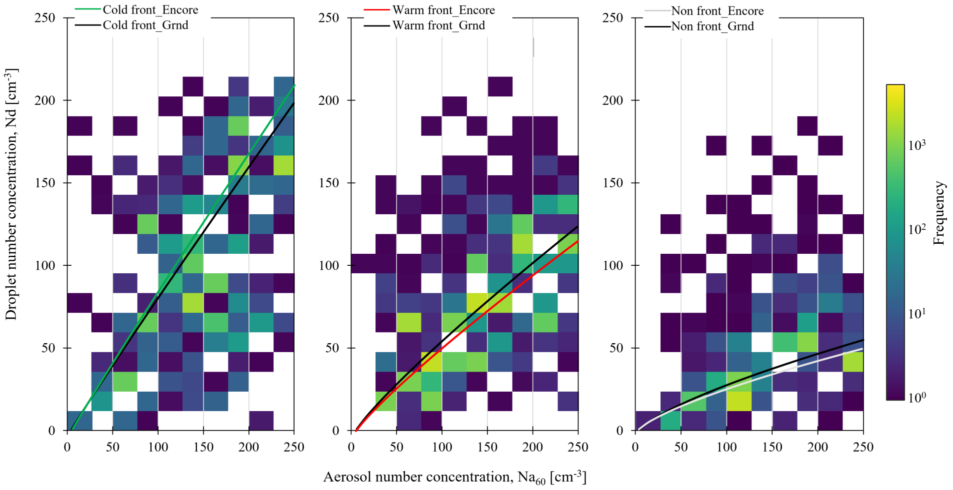

Figure S2: ENCORE droplet number concentration (fit line labelled as Encore) vs MPL droplet number concentration (fit line labelled Grnd) plotted against aerosol concentration N_{60}. The background 2D histogram shows the ENCORE dataset for the 5 days of frontal cloud passages for which it is available for liquid non precipitating and drizzle clouds (max reflectivity of KaZR is 0 to -35 dBZ).

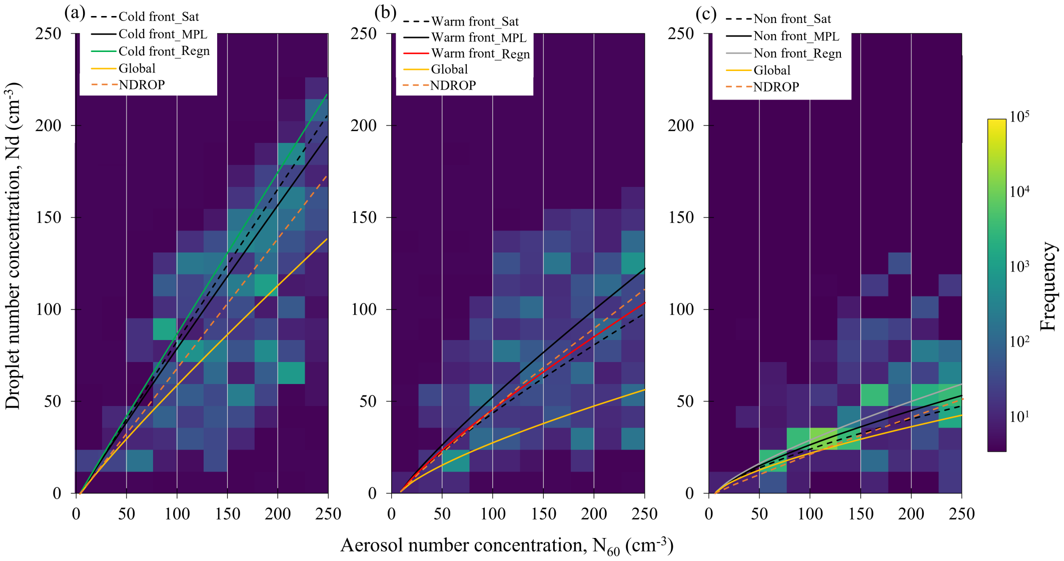

Figure S3: Power-law fits for droplet number concentration against aerosol concentration N_{60} for (a) cold front, (b) warm front and (c) non-frontal clouds. The background 2D histogram shows the MPL dataset for all of 50 frontal cloud cases with only non-precipitating clouds (no drizzle with KaZR max. reflectivity of <-15 dBZ). NDROP is not certain for drizzle and therefore will not justify for use with such conditions otherwise. For observations, aerosol concentration is from UHSAS surface instrument at ARM site in Graciosa.

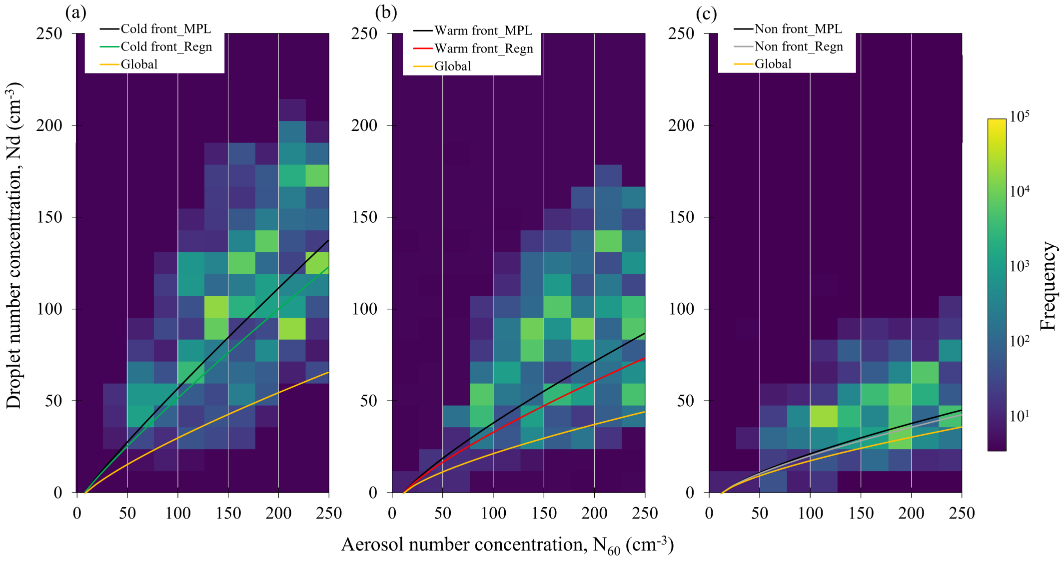

Figure S4: Droplet number concentration plotted against aerosol concentration N_{60}. The background 2D histogram shows the MPL dataset for all of 50 frontal cloud cases with only drizzling clouds (KaZR max. reflectivity of -15< Z <0 dBZ). NDROP is not certain for drizzle and therefore not plotted.

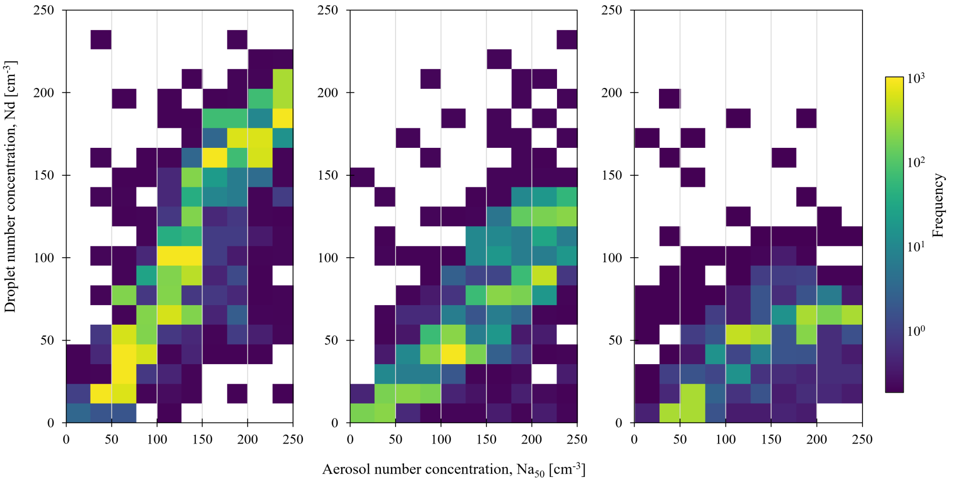

Figure S5: Two-dimensional histogram between cloud droplet number concentration (N_d) and total aerosol number concentration (N_a) derived from the regional UK Met Office Unified Model (UM) simulations. The distribution illustrates the simulated fraction of aerosols that activate into cloud droplets under different cloud regimes, serving as a diagnostic of aerosol activation efficiency. Regions with higher N_d/N_a indicate stronger activation (typically associated with higher supersaturation due to updrafts in frontal clouds), while lower ratios reflect weaker activation and less aerosol-to-droplet conversion.

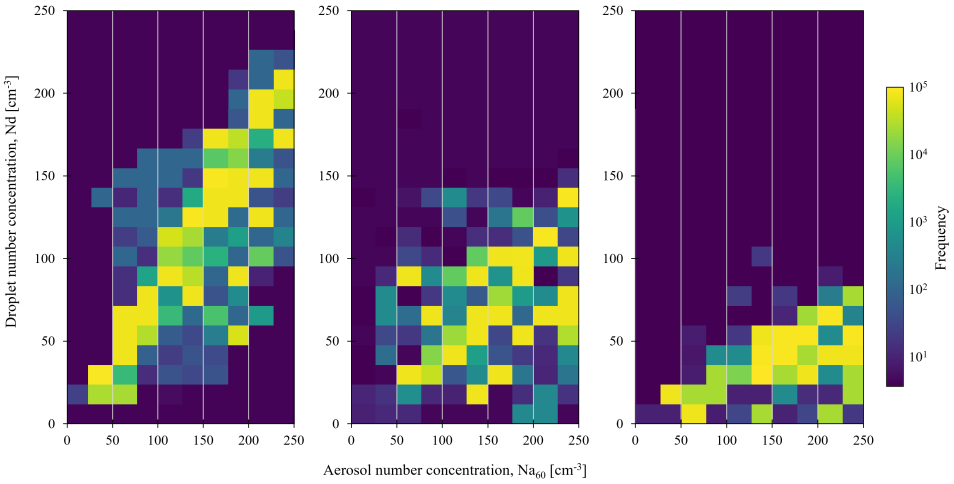

Figure S6: SEVIRI satellite N_d/N_a 2D histogram with N_d derived from CM-SAF Meteosat CPP product and aerosol from surface UHSAS.

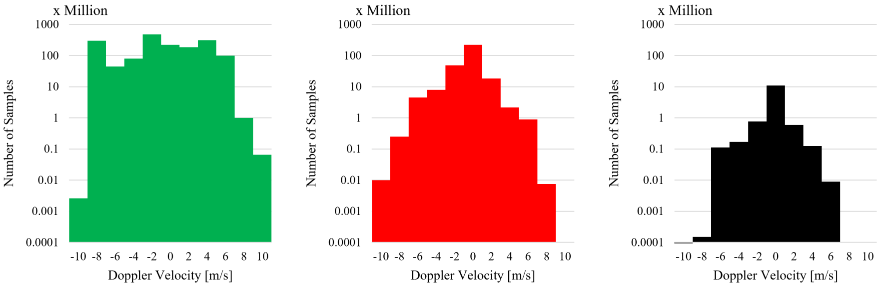

Figure S7: One-dimensional histograms of Doppler velocity retrieved from the Ka-band ARM Zenith Radar (KaZR–ARSCL) at the ARM ENA site, comparing (a) cold frontal, (b) warm frontal, and (c) non-frontal cloud cases. The distributions illustrate differences in vertical air motion among cloud regimes, where broader or more skewed Doppler velocities in frontal clouds indicate stronger updrafts and enhanced turbulence relative to non-frontal conditions. These contrasts provide additional dynamical context for interpreting variations in droplet activation and microphysics across regimes.

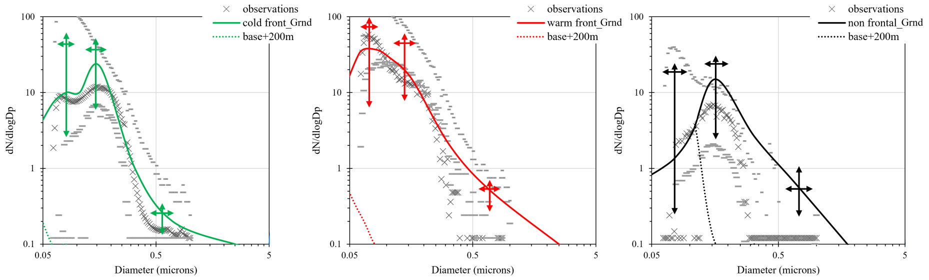

Figure S8: Aerosol size distribution for frontal and non-frontal clouds. Solid lines correspond to simulations with the regional model. Grey 'x' scatter points correspond to UHSAS averaged observations across 50 cyclone cases and '-' scatter points denote minima and maxima observed across the entire test case series for each given diameter. Arrows show standard deviation, representing variability.

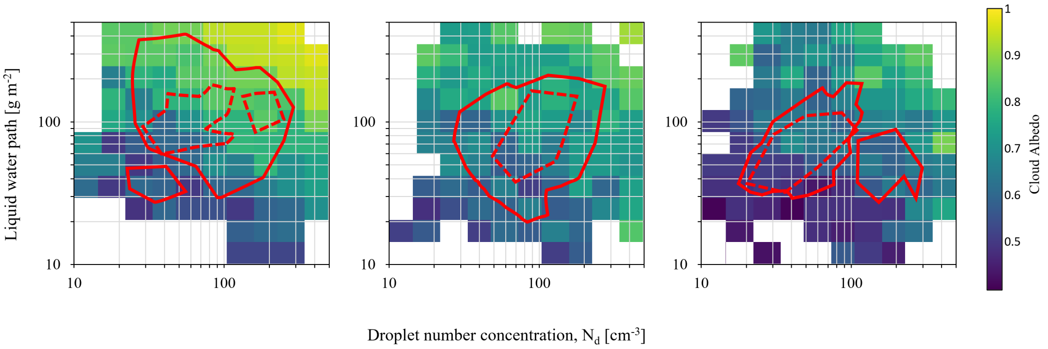

Figure S9: Median cloud albedo with respect to liquid water path and droplet number concentration using SEVIRI satellite observations to infer terms $\frac{\partial A}{\partial \ln Nd}$ and $\frac{\partial A}{\partial \ln LWP}$. The first column for cold front clouds, second column for warm front clouds and third column for non frontal clouds. Red solid contours denote 2-D histogram sample-density thresholds of 0.4%, and dashed red denote 1.6% of the total dataset.

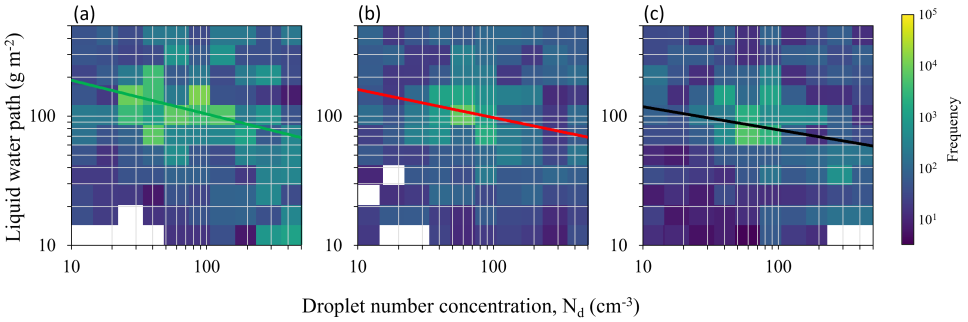

Figure S10: Linear fit for liquid water path against droplet number concentration on log-scaled axis plots for the term $\frac{d \ln LWP}{d \ln Nd}$. The N_d is based on the MPL retrieval and LWP from MWR. This plot includes all non-precipitating and drizzling clouds. The first column shows (a) cold front clouds, the second column (b) warm front clouds and the third colum (c) non frontal clouds, following the approach of Varble *et al.* [10]

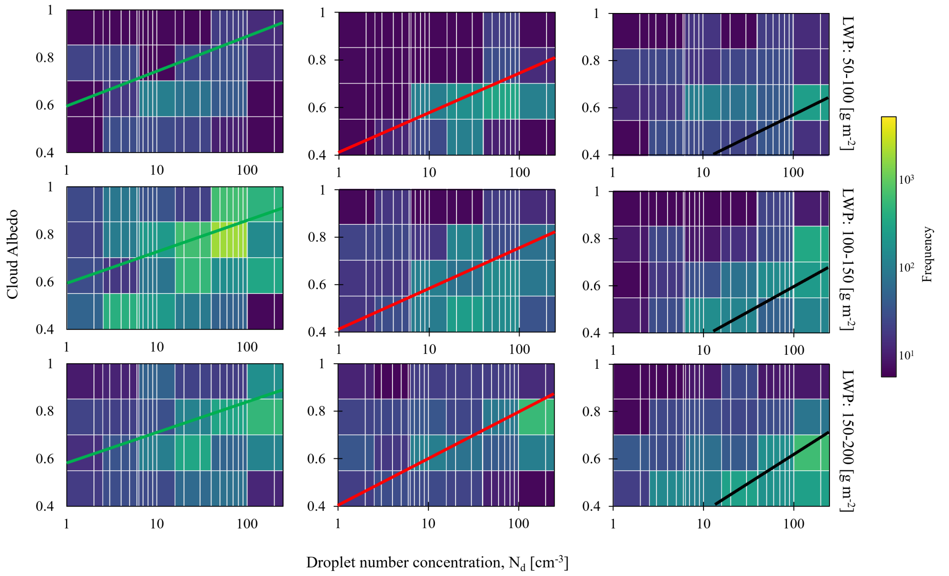

Figure S11: Linear fits for cloud albedo against droplet number concentration on a logarithmic axis for term $\frac{\partial A}{\partial \ln Nd}$. The first column is for cold front clouds, the second column for warm front clouds and the third column for non frontal clouds. Each row of subplots corresponds to a specified range of LWP. The fit lines have intercepts that are shared between bins and floating gradients shown in Table S2. The common intercept enables the gradients to be compared more easily but sometimes leads to a slightly poorer fit to the data.

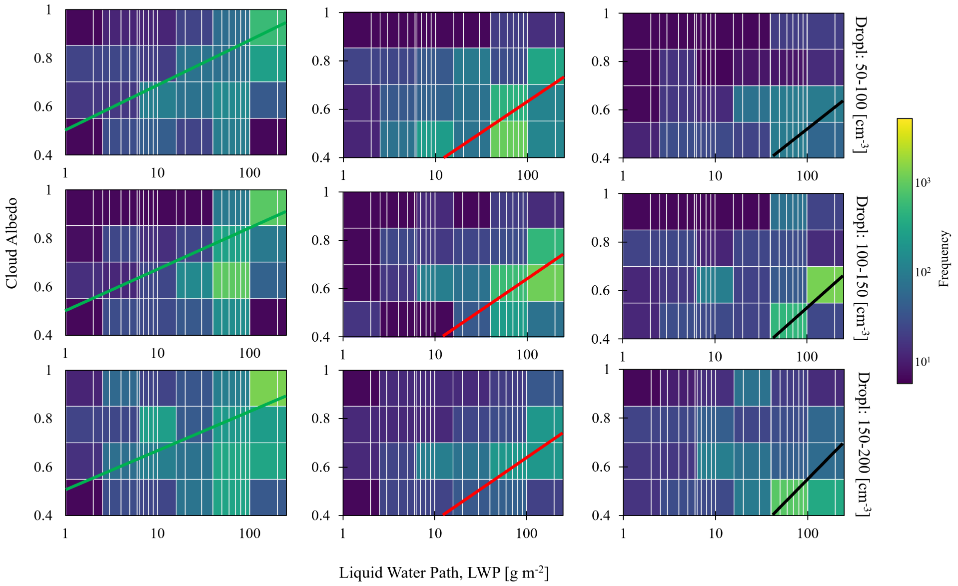

Figure S12: Linear fits for cloud albedo against liquid water path on logarithmic axis for term $\frac{\partial A}{\partial \ln LWP}$. The first column is for cold front clouds, the second column for warm front clouds and the third column for non frontal clouds. Each row of subplots corresponds to a specified range of N_d. The fit lines have intercepts that are shared between bins and floating gradients shown in Table S2. The common intercept enables the gradients to be compared more easily but sometimes leads to a slightly poorer fit to the data.

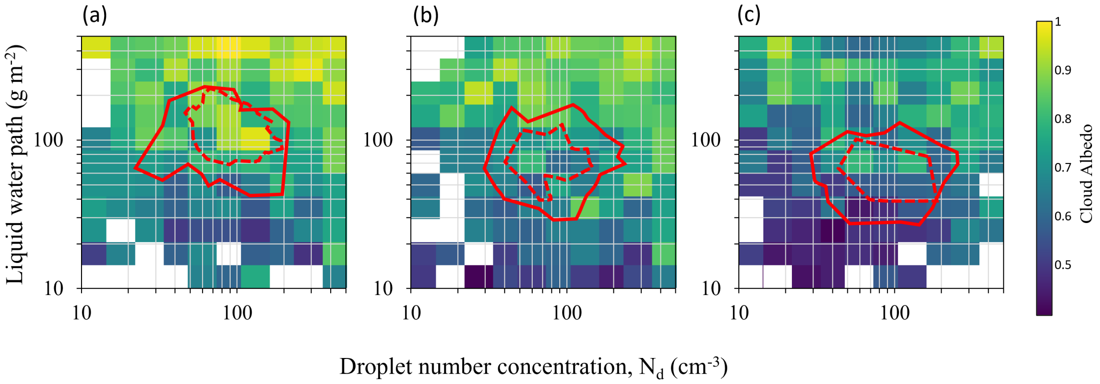

Figure S13: (a-c) Median cloud albedo as a function of liquid water path and droplet number concentration using surface observations to infer $\frac{\partial A}{\partial \ln Nd}$ and $\frac{\partial A}{\partial \ln LWP}$, including only non-precipitating clouds, with maximum column reflectivity $Z < -15$dBZ. The first column shows cold front clouds, the second column warm front clouds and the third column non-frontal clouds. Red solid contours denote 2-D histogram sample-density thresholds of 0.4%, and dashed red denote 1.6% of the total dataset.

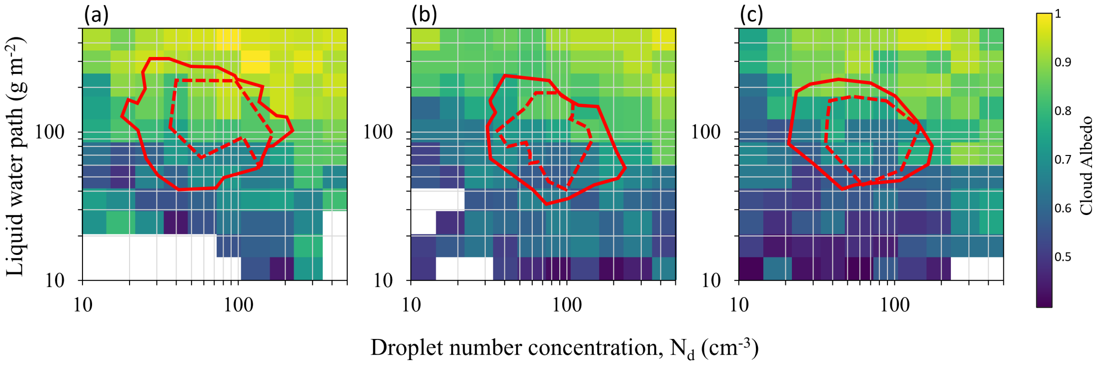

Figure S14: (a-c) Median cloud albedo as a function of liquid water path and droplet number concentration using surface observations to infer $\frac{\partial A}{\partial \ln Nd}$ and $\frac{\partial A}{\partial \ln LWP}$, including only drizzling clouds, with maximum column reflectivity -15$< Z <$0 dBZ. The first column shows cold front clouds, the second column warm front clouds and the third column non-frontal clouds. Red solid contours denote 2-D histogram sample-density thresholds of 0.4%, and dashed red denote 1.6% of the total dataset.

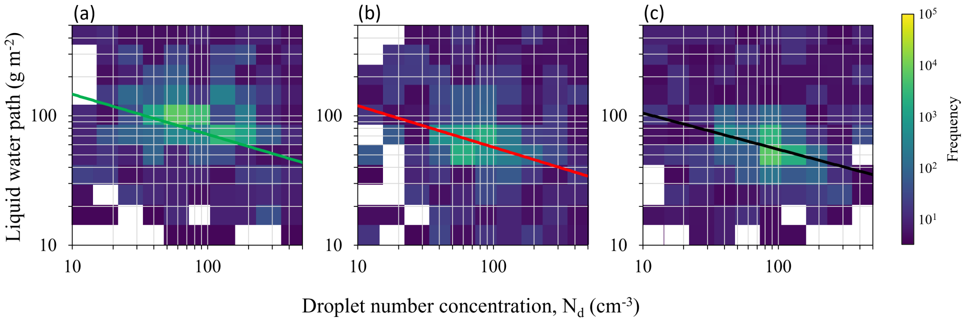

Figure S15: Linear fit for liquid water path against droplet number concentration on log-scaled axis plots for the term $\frac{d \ln LWP}{d \ln Nd}$. The N_d is based on the MPL retrieval and LWP from MWR. This plot includes only non-precipitating clouds where $Z < -15\,$dBZ. The first column shows (a) cold front clouds, the second column (b) warm front clouds and the third colum (c) non frontal clouds.

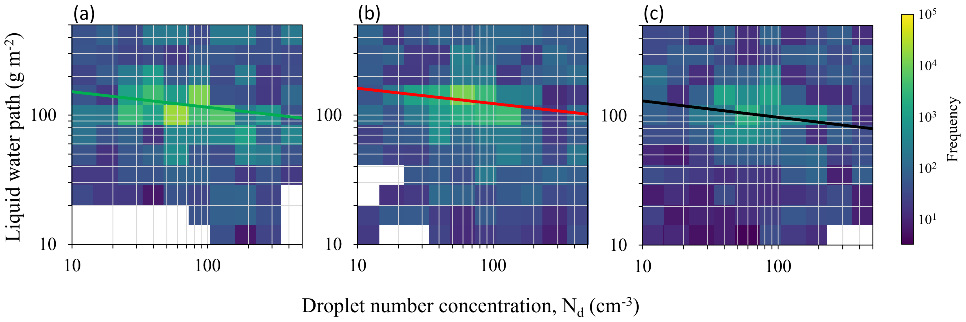

Figure S16: Linear fit for liquid water path against droplet number concentration on log-scaled axis plots for the term $\frac{d \ln LWP}{d \ln Nd}$. The N_d is based on the MPL retrieval and LWP from MWR. This plot includes only drizzling clouds where $-15 < Z < 0\,$dBZ. The first column shows (a) cold front clouds, the second column (b) warm front clouds and the third colum (c) non frontal clouds.

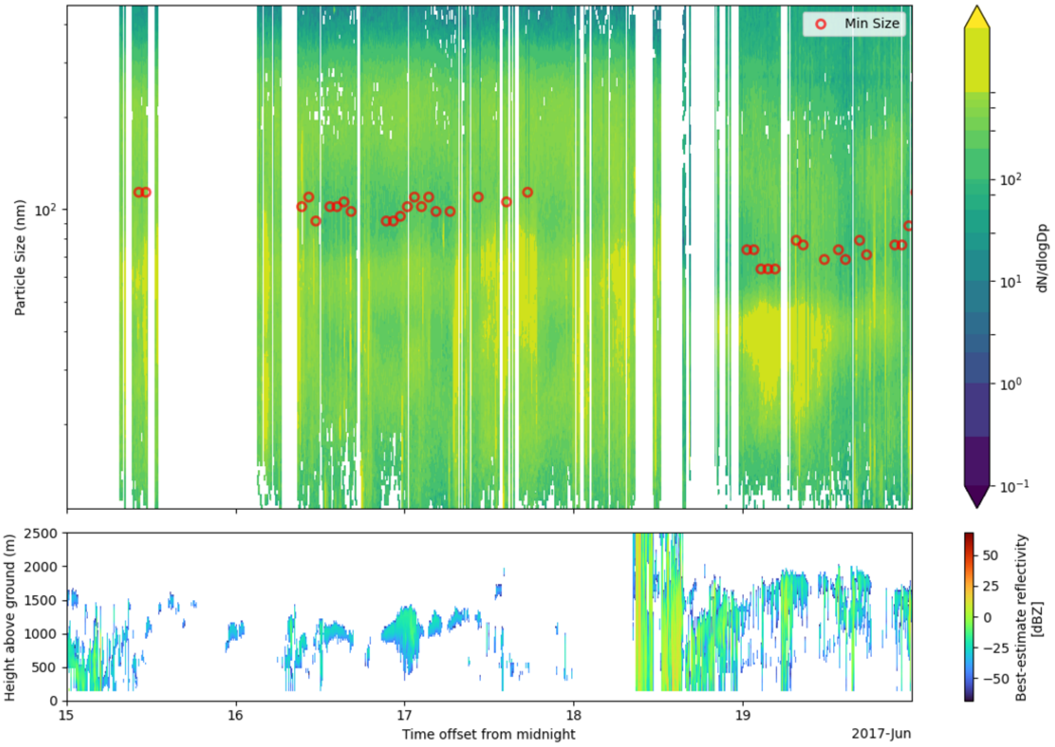

Figure S17: Particle size distribution time series from SMPS data (upper panel) and corresponding KAZR radar reflectivity profiles (lower panel) for June 15–19, 2017. Red circles indicate Hoppel minima identified in 30-minute segments under cloudy conditions. Periods with white vertical bands represent removed data contaminated by rain events or transient aerosol spikes, ensuring cleaner identification of cloud-driven aerosol minima.

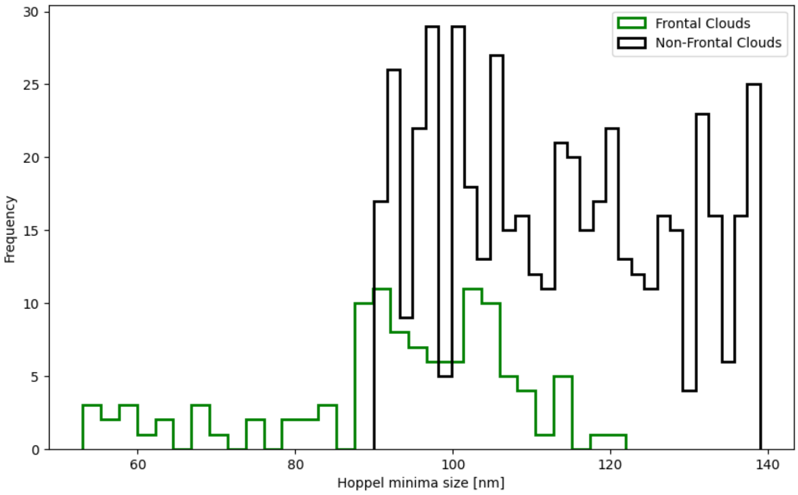

Figure S18: Histogram of Hoppel minimum diameters (in nm) for frontal (green) and non-frontal (black) cloud instances identified in SMPS observations. The Hoppel minimum represents the size at which the aerosol number concentration exhibits a local minimum between the Aitken and accumulation modes, corresponding to particles that have undergone cloud processing and partial activation. The data shown here summarize minima detected within the 50–140 nm size range across all valid and filtered SMPS periods (described in main text), providing a diagnostic comparison of the extent of cloud–aerosol processing and droplet activation between frontal and non-frontal cloud regimes.

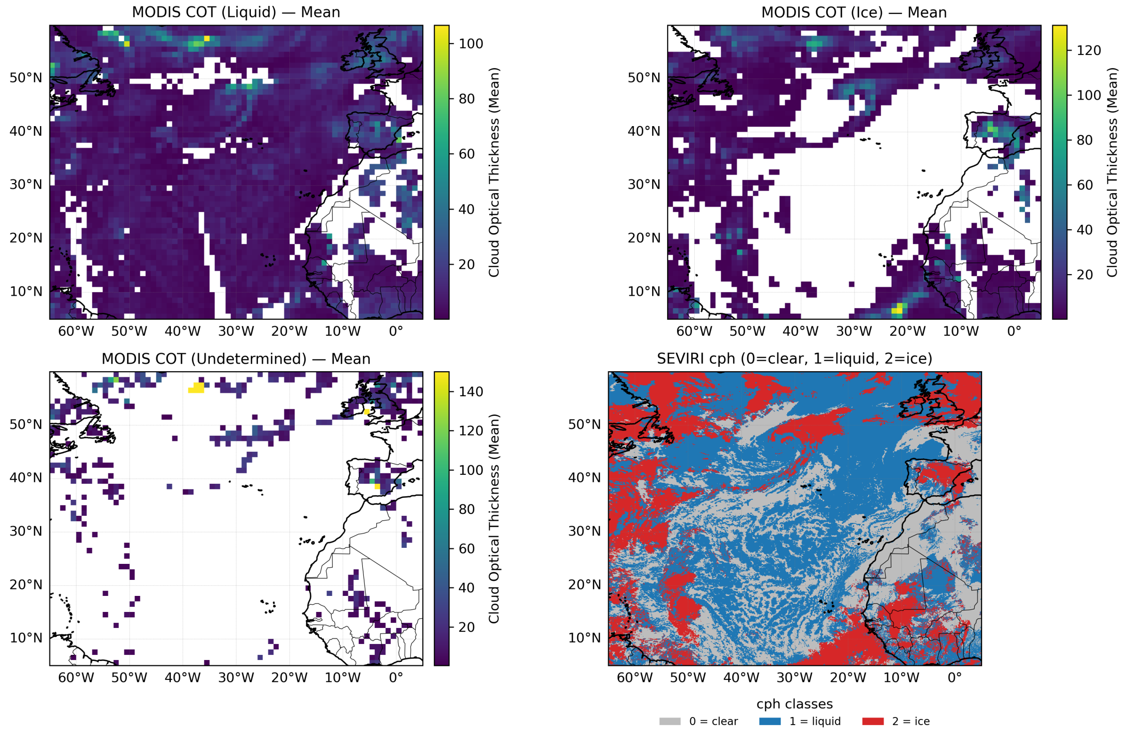

Figure S19: Comparison of cloud-phase information from MODIS and SEVIRI over the Northeast Atlantic (65°W–5°E, 5°–60°N). The three MODIS panels (top-left, top-right, bottom-left) show Level-3 gridded Cloud Optical Thickness (COT) *Mean* for liquid, ice, and undetermined retrievals. The SEVIRI panel (bottom-right) shows the EUMETSAT Cloud Physical Properties (CPP) cloud-phase flag (`cph`). Panels show how the phase implied by MODIS COT components spatially relates to the categorical phase from SEVIRI for the same region and time period.

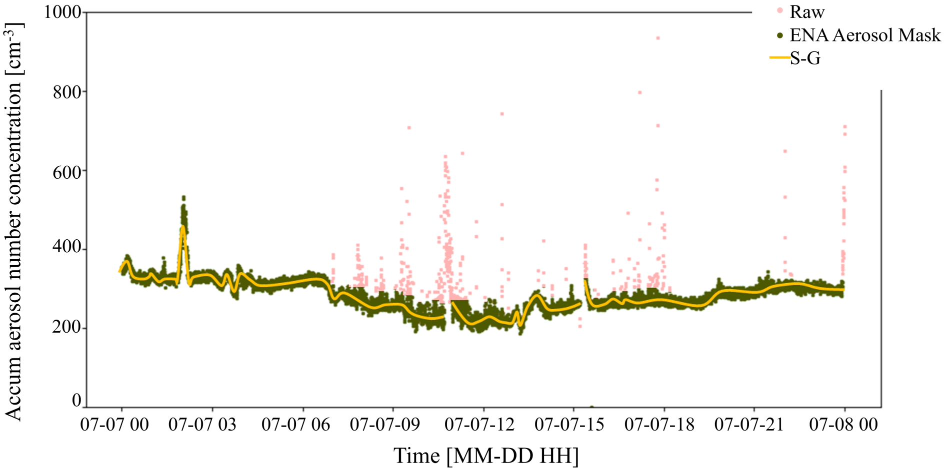

Figure S20: Surface aerosol number concentration measured by the Ultra-High Sensitivity Aerosol Spectrometer (UHSAS), filtered using the Savitzky–Golay (S–G) filter and the ENA Aerosol Mask (ENA-AM).

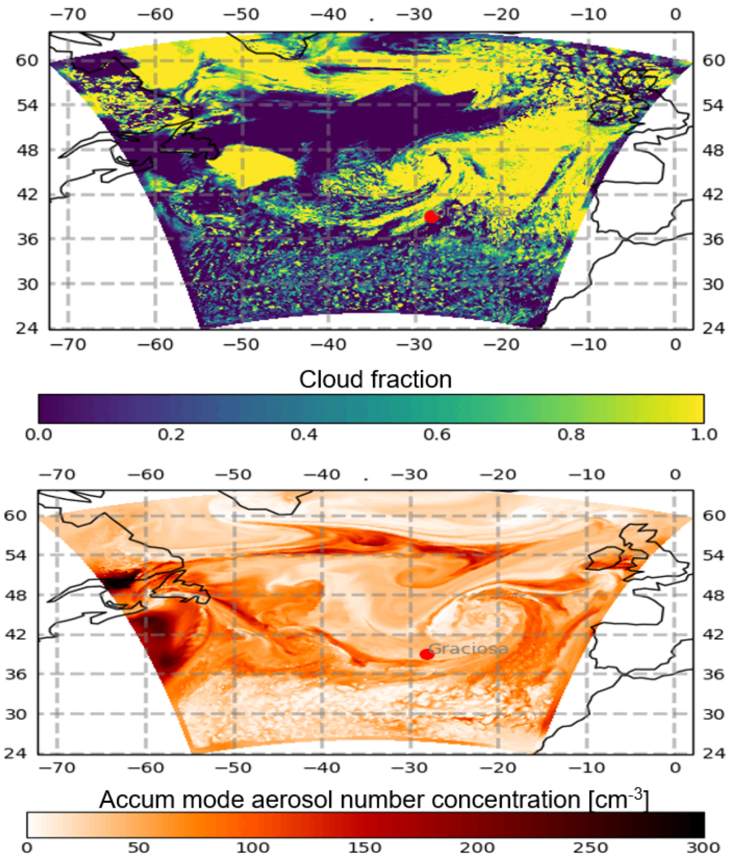

Figure S21: (a) Low cloud fraction and (b) accumulation mode aerosol number concentration diagnostic outputs from UM around Graciosa Island (red dot) during 7th of July 2017 cyclone case.

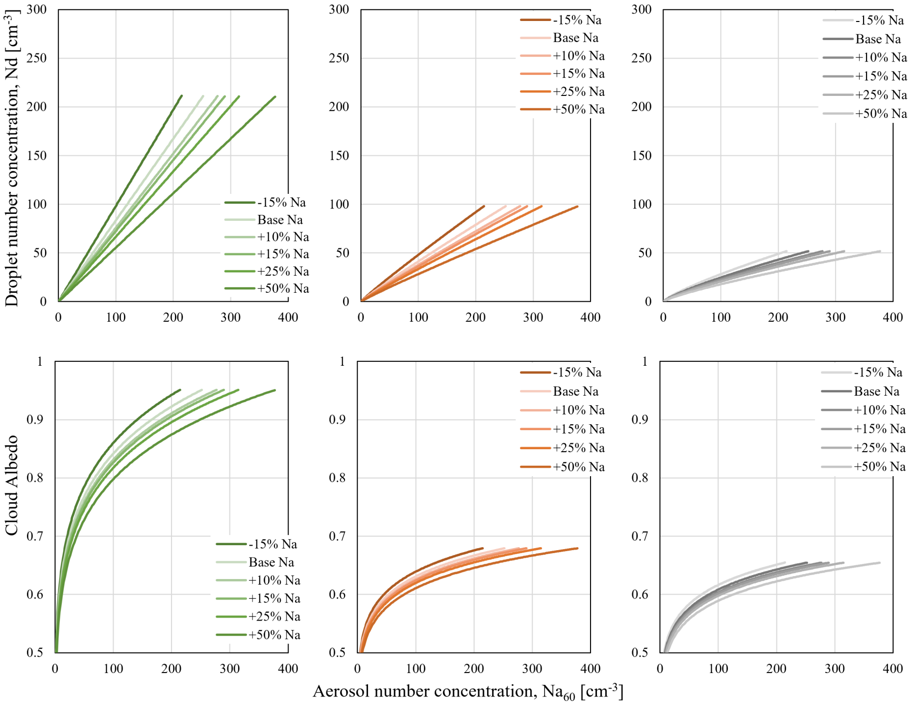

Figure S22: Power-law relationships between droplet number concentration (from NDROP) and cloud albedo (computed using the Lacis equation) versus UHSAS-measured aerosol number concentration (N_{60}) for cold front, warm front, and non-frontal clouds. Each curve tests the sensitivity of the inferred Nd–aerosol and albedo–aerosol relationships to systematic perturbations in the assumed surface aerosol concentration (positive or negative increments from -15% to +50% representing possible under- or overestimation of cloud-base values), thereby testing the robustness of the observed trends across cloud regimes.

References

[1] Feingold, G., Eberhard, W.L., Veron, D.E., Previdi, M.: First measurements of the twomey indirect effect using ground-based remote sensors. Geophysical Research Letters **30**(6) (2003)

[2] McComiskey, A., Feingold, G., Frisch, A.S., Turner, D.D., Miller, M.A., Chiu, J.C., Min, Q., Ogren, J.A.: An assessment of aerosol-cloud interactions in marine stratus clouds based on surface remote sensing. Journal of Geophysical Research: Atmospheres **114**(D9) (2009)

[3] Schmidt, J., Ansmann, A., Bühl, J., Baars, H., Wandinger, U., Mueller, D., Malinka, A.V.: Dual-fov raman and doppler lidar studies of aerosol-cloud interactions: Simultaneous profiling of aerosols, warm-cloud properties, and vertical wind. Journal of Geophysical Research: Atmospheres **119**(9), 5512–5527 (2014)

[4] Kim, B.-G., Miller, M.A., Schwartz, S.E., Liu, Y., Min, Q.: The role of adiabaticity in the aerosol first indirect effect. Journal of Geophysical Research: Atmospheres **113**(D5) (2008)

[5] Feingold, G., Furrer, R., Pilewskie, P., Remer, L.A., Min, Q., Jonsson, H.: Aerosol indirect effect studies at southern great plains during the may 2003 intensive operations period. Journal of Geophysical Research: Atmospheres **111**(D5) (2006)

[6] Ranjithkumar, A., Gordon, H., Williamson, C., Rollins, A., Pringle, K., Kupc, A., Abraham, N.L., Brock, C., Carslaw, K.: Constraints on global aerosol number concentration, so 2 and condensation sink in ukesm1 using atom measurements. Atmospheric Chemistry and Physics **21**(6), 4979–5014 (2021)

[7] Williamson, C.J., Kupc, A., Axisa, D., Bilsback, K.R., Bui, T., Campuzano-Jost, P., Dollner, M., Froyd, K.D., Hodshire, A.L., Jimenez, J.L., *et al.*: A large source of cloud condensation nuclei from new particle formation in the tropics. Nature **574**(7778), 399–403 (2019)

[8] Zheng, G., Wang, Y., Wood, R., Jensen, M.P., Kuang, C., McCoy, I.L., Matthews, A., Mei, F., Tomlinson, J.M., Shilling, J.E., *et al.*: New particle formation in the remote marine boundary layer. Nature communications **12**(1), 527 (2021)

[9] Dedrick, J.L., Russell, L.M., Sedlacek III, A.J., Kuang, C., Zawadowicz, M.A., Lubin, D.: Aerosol-correlated cloud activation for clean conditions in the tropical atlantic boundary layer during lasic. Geophysical Research Letters **51**(3), 2023–105798 (2024)

[10] Varble, A.C., Ma, P.-L., Christensen, M.W., Mülmenstädt, J., Tang, S., Fast, J.: Evaluation of liquid cloud albedo susceptibility in e3sm using coupled eastern north atlantic surface and satellite retrievals. Atmospheric Chemistry and Physics **23**(20), 13523–13553 (2023)